

**QUANTIFICATION OF THREE-DIMENSIONAL
ELASTIC-PLASTIC CRACK-TIP STRESS FIELDS**

NORWAHIDA BINTI YUSOFF

UNIVERSITI SAINS MALAYSIA

2018

**QUANTIFICATION OF THREE-DIMENSIONAL ELASTIC-
PLASTIC CRACK-TIP STRESS FIELDS**

by

NORWAHIDA BINTI YUSOFF

**Thesis submitted in fulfilment of the
requirements for the degree of
Doctor of Philosophy**

June 2018

ACKNOWLEDGEMENT

In the name of Allah, the Most Gracious, the Most Merciful.

All praises and thanks are due to the Almighty Allah for giving me strength and blessings to complete this thesis. My deepest gratitude goes to my supervisor, Dr. Feizal Yusof, for his continuous and tremendous guidance, encouragement and support throughout the research work. His approach in problem solving and attention to detail has pushed me to strive for the best, which I believe is the key to the success of this research, and to the completion of this thesis.

I would like to express my sincere appreciation to Dr.-Ing Muhammad Razi Abdul Rahman for his technical support on the High Performance Computing (HPC), and to all technical staff, particularly, En. Fakruruzi Fadzil for his help in conducting the experiments. Acknowledgements are also due to University of Science Malaysia and Ministry of Higher Education for the award of an academic training fellowship which enables the research to be carried out.

Lastly, but never the least, my highest appreciation goes to my husband, Wan Mohd Rathnor, for being a shoulder to lean on throughout this journey. After all, this thesis is mostly dedicated to my children, Hadiff, Aqeela, and Hatta, who have always been my source of motivation and joy. I would also like to dedicate this thesis to my father, my late mother, and my mother-in-law for their unconditional love and support. My appreciation also goes to all my siblings who have reminded me how much I am loved and cared with their endless support and encouragement.

TABLE OF CONTENTS

| | Page |
|--|-------------|
| ACKNOWLEDGEMENT | ii |
| TABLE OF CONTENTS | iii |
| LIST OF TABLES | vi |
| LIST OF FIGURES | vii |
| LIST OF ABBREVIATIONS | xviii |
| LIST OF SYMBOLS | xix |
| ABSTRAK | xxii |
| ABSTRACT | xxiv |
| | |
| CHAPTER ONE: INTRODUCTION | |
| 1.1 Background | 1 |
| 1.2 Problem Statement | 3 |
| 1.3 Objectives of Research | 4 |
| 1.4 Scope of Research Work | 5 |
| 1.5 Thesis Outline | 7 |
| | |
| CHAPTER TWO: LITERATURE REVIEW | |
| 2.1 Analytical Fracture Mechanics | 8 |
| 2.1.1 Two-Dimensional Crack-tip Fields | 9 |
| 2.1.1(a) T-stress | 20 |
| 2.1.1(b) K/J-T Approach | 22 |
| 2.1.1(c) J-Q Approach | 23 |
| 2.1.1(d) J-A ₂ Approach | 25 |

| | | |
|----------|---|----|
| 2.1.2 | Two-Dimensional Crack-tip in Perfect Plasticity | 25 |
| 2.1.2(a) | Prandtl Slip Lines | 26 |
| 2.1.2(b) | Plane Stress Slip Lines | 29 |
| 2.1.2(c) | Blunted Crack-Tip Fields | 32 |
| 2.1.3 | Three-Dimensional Crack-tip Fields | 36 |
| 2.1.3(a) | Elastic-Plastic Stress Fields | 36 |
| 2.1.3(b) | Three-dimensional Crack-Tip Constraint | 37 |
| 2.1.3(c) | Quantification of Three-dimensional Constraint Loss | 39 |
| 2.1.3(d) | Corner Field | 51 |
| 2.2 | Experimental Fracture Mechanics | 54 |
| 2.2.1(a) | Measurement of Crack-Tip Deformation | 54 |
| 2.2.1(b) | Digital Image Correlation | 57 |
| 2.3 | Summary | 59 |

CHAPTER THREE: METHODOLOGY

| | | |
|-------|---|----|
| 3.1 | Numerical Methods | 61 |
| 3.1.1 | Boundary Layer Formulations | 62 |
| 3.1.2 | Full-field Compact Tension Specimen Model | 69 |
| 3.1.3 | Material Response | 73 |
| 3.1.4 | Computational Procedures | 78 |
| 3.1.5 | Post-processing Procedures | 79 |
| 3.1.6 | Validation of Crack-tip Fields | 80 |
| 3.2 | Experimental Procedures for Measuring Crack-Tip Deformation | 85 |
| 3.3 | Summary | 93 |

CHAPTER FOUR: RESULTS AND DISCUSSION

| | | |
|-----|---|-----|
| 4.1 | Three-dimensional Crack-tip Deformation | 96 |
| 4.2 | Three-Dimensional Crack-tip Border Fields | 100 |

| | | |
|-------|---|-----|
| 4.2.1 | Asymptotic Crack-tip Fields ($r = 0$) | 100 |
| 4.2.2 | Three-dimensional Fields within the Micro-Separation Distance $2J/\sigma_0 \leq r \leq 5J/\sigma_0$ | 117 |
| 4.2.3 | Stress Field Ahead of the Crack Front | 127 |
| 4.3 | Elastic-Plastic Corner Fields | 135 |
| 4.3.1 | Asymptotic Perfectly-Plastic Corner Stress Fields | 136 |
| 4.3.2 | Experimental Determination of Corner Deformation Fields | 139 |
| 4.3.3 | Strain-Hardening Corner Stress Fields | 157 |
| 4.4 | Quantification of Three-dimensional Constraint Loss | 159 |
| 4.4.1 | Through-thickness Description of σ_{00} and σ_m | 159 |
| 4.4.2 | The Sensitivity Constant, γ | 163 |
| 4.5 | Analytical Solutions for Three-Dimensional Crack-tip Fields | 168 |
| 4.5.1 | Governing Equations | 169 |
| 4.5.2 | The Proposed Scalar $\Delta\sigma$ | 171 |
| 4.5.3 | Analytical Three-Dimensional Crack-Tip Fields | 173 |
| 4.5.4 | Verification of the Analytical Solutions | 178 |
| 4.6 | Summary | 183 |

CHAPTER FIVE: CONCLUSION AND RECOMMENDATIONS

| | | |
|-----|--------------|-----|
| 5.1 | Summary | 185 |
| 5.2 | Future Works | 188 |

| | |
|-------------------|-----|
| REFERENCES | 189 |
|-------------------|-----|

APPENDICES

LIST OF PUBLICATIONS

LIST OF TABLES

| | | Page |
|-----------|---|-------------|
| Table 2.1 | Methods of experimental fracture mechanics. | 55 |
| Table 3.1 | Mechanical properties of AISI 316L stainless steel | 77 |
| Table 3.2 | Summary of duration taken to complete a finite element analysis with respect to the total variables generated and the number of processor used. | 78 |
| Table 4.1 | Values of the constants in Equation (4.1). | 97 |
| Table 4.2 | Local deformations along the crack front of CT specimen characterized in terms of μ for (a) $B/(W-a) = 1$, (b) $B/(W-a) = 0.5$, and (c) $B/(W-a) = 0.12$, at range of load levels, P/P_0 . | 99 |

LIST OF FIGURES

| | | Page |
|-------------|--|-------------|
| Figure 1.1 | The overall scope of the current research work. | 5 |
| Figure 2.1 | Seminal works in the development of fracture mechanics concept in continuum mechanics. | 9 |
| Figure 2.2 | Elliptical hole in an infinite plate. | 10 |
| Figure 2.3 | Coordinate axis ahead of a crack-tip used in Westergaard asymptotic solution. | 11 |
| Figure 2.4 | Three modes of deformation. | 12 |
| Figure 2.5 | Irwin plastic zone correction. | 14 |
| Figure 2.6 | Dugdale's strip yield plastic zones. | 14 |
| Figure 2.7 | The crack-tip opening displacement measured from (a) crack mouth opening displacement, and (b) at the intersection of 90° vertex with the crack flanks. | 15 |
| Figure 2.8 | Arbitrary contour around a crack-tip. | 17 |
| Figure 2.9 | The slip line fields for (a) centre crack in tension, (b) double edge crack in tension. | 18 |
| Figure 2.10 | The hoop stress directly ahead of the crack-tip in boundary layer formulations as a function of T/σ_0 after Betegón and Hancock (1991). | 22 |
| Figure 2.11 | Prandtl slip line field. | 26 |

| | | |
|-------------|---|----|
| Figure 2.12 | Asymptotic cylindrical stresses in the Prandtl slip field after Du and Hancock (1991). | 28 |
| Figure 2.13 | The sector configuration for the Hutchinson plane stress field. | 29 |
| Figure 2.14 | Plane stress asymptotic stresses in a perfectly-plastic material after Hutchinson (1968a). | 30 |
| Figure 2.15 | Plane stress mode-I asymptotic field configuration after Sham and Hancock (1999), with $\theta_I = 39.126^\circ$. | 30 |
| Figure 2.16 | Asymptotic (a) Cartesian and, (b) cylindrical stresses of Sham and Hancock (1999) plane stress field. | 32 |
| Figure 2.17 | The difference between finite and small strain analyses at distance $0 < r < 2J/\sigma_0$ after McMeeking and Parks (1979). | 33 |
| Figure 2.18 | Modification of slip line field in near tip region due to crack-tip blunting after Rice and Johnson (1969). | 34 |
| Figure 2.19 | The approximate modified stress distribution due to large tip geometry changes as function of initial yield strain, σ_0/E , and hardening exponent, N , after Rice and Johnson (1969). | 35 |
| Figure 2.20 | Global constraint factor, α_g , for (a) various specimen types with $c/B > 4$, and (b) thick specimens with $c/B \leq 4$ after Newman et al. (1994) | 41 |
| Figure 2.21 | Comparison between the through-thickness variation of T_z from Equation (2.47) and the finite element results of Nakamura and Parks (1990) after W. Guo (1995). | 44 |
| Figure 2.22 | Normalized fracture toughness as a function of unified measure of constraint, ϕ , after Mostafavi et al. (2010). | 48 |
| Figure 2.23 | Normalized $J_{IC}-\sqrt{A_p}$ locus for specimens with different in-plane and out-of-plane constraint levels after J. Yang et al. (2013) | 50 |

| | | |
|-------------|--|----|
| Figure 2.24 | Corner singularity coordinate system. | 51 |
| Figure 2.25 | Comparison of the out-of-plane displacements obtained numerically and experimentally at (a) $\theta = 0^\circ$, and (b) $\theta = 30^\circ$, after Hom and McMeeking (1990). | 52 |
| Figure 2.26 | Comparison between the cylindrical stresses for 3D non-hardening solution and those of the 2D plane stress solution after Yusof and Hancock (2005). | 53 |
| Figure 2.27 | Reference subset and target subset chosen from undeformed and deformed images, respectively | 58 |
| Figure 3.1 | The circular disk representing the near crack front region of a thin plate. | 62 |
| Figure 3.2 | The finite element meshes of the quarter-model of thin plate boundary layer formulations SGC sharp crack-tip models. | 65 |
| Figure 3.3 | The finite element meshes of the quarter-model of blunted crack-tip model. | 67 |
| Figure 3.4 | Geometry of the CT specimen. | 69 |
| Figure 3.5 | Three-dimensional full-field models of CT specimens of (a) $B/(W-a) = 1$, (b) $B/(W-a) = 0.5$, and (c) $B/(W-a) = 0.12$. | 70 |
| Figure 3.6 | Blunted tip of a CT specimen. | 71 |
| Figure 3.7 | Displacement u_2 was applied on the node joining four elements that represent the loading pin. | 72 |
| Figure 3.8 | The subsize rectangular tension test specimen following the ASTM E8M standard. All dimensions are in (mm) | 75 |
| Figure 3.9 | Stress-strain curve for AISI 316L stainless steel obtained from one of three tensile tests; curve (a) shows the values of | 76 |

tensile strength and total elongation, and curve (b) shows the values of modulus of elasticity and yield strength.

| | | |
|-------------|--|----|
| Figure 3.10 | The plastic part of the power-law relation (Equation (3.12)) fitted the uniaxial stress-stain data of 316L stainless steel with the value of n close to 6. | 77 |
| Figure 3.11 | The asymptotic stresses for the SGC solution, compared with the Prandtl field. | 81 |
| Figure 3.12 | The hoop stress, $\sigma_{\theta\theta}$, ahead of crack-tip for the LGC solution, compared with the HRR plane strain field ($n = \infty$) | 81 |
| Figure 3.13 | The asymptotic stresses for the full-field $B/(W-a) = 1$ CT specimen, compared with the Prandtl field. | 83 |
| Figure 3.14 | The hoop stress, $\sigma_{\theta\theta}$, ahead of crack-tip under small-scale yielding and full-plasticity conditions for the full-field $B/(W-a) = 1$ CT specimen, compared with the HRR plane strain fields. | 84 |
| Figure 3.15 | The configuration of CT specimen following the ASTM E399 (ASTM, 2012) standard. All dimensions are in (mm). | 85 |
| Figure 3.16 | Schematic representation of a 2D DIC experimental setup. | 86 |
| Figure 3.17 | Experimental configuration for DIC image recording. | 87 |
| Figure 3.18 | Image of the surface of the $B/(W-a) = 0.5$ CT specimen captured at zero load in a 1600 x 1200 pixels frame. | 88 |
| Figure 3.19 | A sequence of 883 x 808 pixels patches of the region of interest on the surface of the $B/(W-a) = 0.5$ CT specimen at (a) 1250 N, (b) 2500 N, (c) 3750 N, and (d) 5000 N. | 89 |
| Figure 3.20 | The steps written in Fortran code for acquiring the required displacement and strain fields. | 90 |

| | | |
|-------------|--|-----|
| Figure 3.21 | Process of data extraction from DIC imaging and processing to Fortran data array. | 92 |
| Figure 4.1 | The variation of normalized local J along the crack front as a function of load levels. | 96 |
| Figure 4.2 | The asymptotic Cartesian stress fields for the SGC boundary layer formulations, (a) at the midplane ($x_3/t = 0$), (b) near the quarter-plane ($x_3/t = 0.26$), and (c) near the free-surface ($x_3/t = 0.485$). | 102 |
| Figure 4.3 | The asymptotic cylindrical stress fields for the SGC boundary layer formulations, (a) at the midplane ($x_3/t = 0$), (b) near the quarter-plane ($x_3/t = 0.26$), and (c) near the free-surface ($x_3/t = 0.485$). | 103 |
| Figure 4.4 | The asymptotic mean stress σ_m for the SGC boundary layer formulation at the midplane, and near the free-surface. | 104 |
| Figure 4.5 | The asymptotic out-of-plane direct stress σ_{33} for the SGC boundary layer formulation at the midplane, and near the free-surface. | 105 |
| Figure 4.6 | The asymptotic out-of-plane shear stress σ_{13} for the SGC boundary layer formulation at the midplane, and near the free-surface. | 105 |
| Figure 4.7 | The asymptotic out-of-plane shear stress σ_{23} for the SGC boundary layer formulation at the midplane, and near the free-surface. | 106 |
| Figure 4.8 | The asymptotic deviatoric stress $s_{\theta\theta}$ in the leading sector $0^\circ \leq \theta \leq 45^\circ$ at different sections along crack front, and at all load levels for the SGC boundary layer formulations. | 107 |
| Figure 4.9 | Cylindrical stresses $B/(W-a) = 1$ CT specimen (a) at the midplane ($x_3/t = 0$), (b) near the quarter-plane ($x_3/t = 0.26$), and (c) near the free-surface ($x_3/t = 0.485$). | 108 |

| | | |
|-------------|--|-----|
| Figure 4.10 | Cylindrical stresses for $B/(W-a) = 0.5$ CT specimen (a) at the midplane ($x_3/t = 0$), (b) near the quarter-plane ($x_3/t = 0.256$), and (c) near the free-surface ($x_3/t = 0.484$). | 109 |
| Figure 4.11 | Cylindrical stresses for $B/(W-a) = 0.12$ CT specimen (a) at the midplane ($x_3/t = 0$), (b) near the quarter-plane ($x_3/t = 0.3$), and (c) near the free-surface ($x_3/t = 0.467$). | 110 |
| Figure 4.12 | Through-thickness variations of the asymptotic mean stress, σ_m for (a) $B/(W-a) = 1$, (b) $B/(W-a) = 0.5$, and (c) $B/(W-a) = 0.12$ CT specimens. | 112 |
| Figure 4.13 | Through-thickness variations of the asymptotic out-of-plane direct stress, σ_{33} for (a) $B/(W-a) = 1$, (b) $B/(W-a) = 0.5$, and (c) $B/(W-a) = 0.12$ CT specimens. | 113 |
| Figure 4.14 | Through-thickness variations of the asymptotic out-of-plane direct stress, σ_{23} for (a) $B/(W-a) = 1$, (b) $B/(W-a) = 0.5$, and (c) $B/(W-a) = 0.12$ CT specimens. | 114 |
| Figure 4.15 | Through-thickness variations of the asymptotic out-of-plane direct stress, σ_{13} for (a) $B/(W-a) = 1$, (b) $B/(W-a) = 0.5$, and (c) $B/(W-a) = 0.12$ CT specimens. | 115 |
| Figure 4.16 | The asymptotic deviatoric stress $s_{\theta\theta}$ in the leading sector $0^\circ \leq \theta \leq 45^\circ$ at different sections along the crack front of all CT specimens. | 116 |
| Figure 4.17 | The angular distribution of the hoop stress, $\sigma_{\theta\theta}$, at (a) $r = 2J/\sigma_o$, and (b) $r = 5J/\sigma_o$ in different sections along the crack front for the SGC boundary layer formulations at $\Omega_{far} = 8$. | 118 |
| Figure 4.18 | The angular distribution of the mean stress, σ_m , at (a) $r = 2J/\sigma_o$, and (b) $r = 5J/\sigma_o$ in different sections along the crack front for the SGC boundary layer formulations at $\Omega_{far} = 8$. | 119 |
| Figure 4.19 | The maximum stress deviator, $s_{\theta\theta}$, at $r = 2J/\sigma_o$ and $r = 5J/\sigma_o$ in the leading sector $0^\circ \leq \theta \leq 45^\circ$ in different sections along the crack front for the SGC boundary layer formulations at $\Omega_{far} = 8$. | 120 |

| | | |
|-------------|--|-----|
| Figure 4.20 | The angular distribution of the hoop stress, $\sigma_{\theta\theta}$, at (a) $r = 2J/\sigma_o$, and (b) $r = 5J/\sigma_o$ in different sections along the crack front of $B/(W-a)=1$ CT specimen at $\mu_{loc} = 29.74$. | 122 |
| Figure 4.21 | The angular distribution of the mean stress, σ_m , at (a) $r = 2J/\sigma_o$, and (b) $r = 5J/\sigma_o$ in different sections along the crack front of $B/(W-a)=1$ CT specimen at $\mu_{loc} = 29.74$. | 122 |
| Figure 4.22 | The angular distribution of the hoop stress, $\sigma_{\theta\theta}$, at (a) $r = 2J/\sigma_o$, and (b) $r = 5J/\sigma_o$ in different sections along the crack front of $B/(W-a)=0.5$ CT specimen at $\mu_{loc} = 29.17$. | 123 |
| Figure 4.23 | The angular distribution of the mean stress, σ_m , at (a) $r = 2J/\sigma_o$, and (b) $r = 5J/\sigma_o$ in different sections along the crack front of $B/(W-a)=0.5$ CT specimen at $\mu_{loc} = 29.17$. | 124 |
| Figure 4.24 | The angular distribution of the hoop stress, $\sigma_{\theta\theta}$, at (a) $r = 2J/\sigma_o$, and (b) $r = 5J/\sigma_o$ in different sections along the crack front of $B/(W-a)=0.12$ CT specimen at $\mu_{loc} = 29.56$. | 125 |
| Figure 4.25 | The angular distribution of the mean stress, σ_m , at (a) $r = 2J/\sigma_o$, and (b) $r = 5J/\sigma_o$ in different sections along the crack front of $B/(W-a)=0.12$ CT specimen at $\mu_{loc} = 29.56$. | 126 |
| Figure 4.26 | The maximum stress deviator, $s_{\theta\theta}$, at $r = 2J/\sigma_o$ and $r = 5J/\sigma_o$ in the leading sector $0^\circ \leq \theta \leq 45^\circ$ in different sections along the crack front of CT specimens of different thicknesses at the highest local deformation μ_{loc} . | 127 |
| Figure 4.27 | The hoop stress, $\sigma_{\theta\theta}$, ahead of the crack-tip at the midplane of the boundary layer formulations of the SGC (markers without line) and the LGC (solid line with markers). | 128 |
| Figure 4.28 | The mean stress, σ_m , ahead of the crack-tip at the midplane of the boundary layer formulations of the SGC (markers without line) and the LGC (solid line with markers). | 128 |
| Figure 4.29 | The hoop stress, $\sigma_{\theta\theta}$, ahead of the crack-tip at four different section $x3/t = 0, 0.26, 0.4, 0.485$ along the crack front of the boundary layer formulations of the SGC and LGC at $\Omega_{far} = 8$. | 130 |

| | | |
|-------------|--|-----|
| Figure 4.30 | The mean stress, σ_m , ahead of the crack-tip at four different section $x3/t = 0, 0.26, 0.4, 0.485$ along the crack front of the boundary layer formulations of the SGC and LGC at $\Omega_{far} = 8$. | 130 |
| Figure 4.31 | The maximum stress deviator, $s_{\theta\theta}$, ahead of the crack front at the midplane and near the free-surface of the boundary layer formulations of the LGC model at $\Omega_{far} = 1, 3, 5, \text{ and } 8$. | 131 |
| Figure 4.32 | The hoop stress, $\sigma_{\theta\theta}$, directly ahead of the crack-tip ($\theta = 0^\circ$) in four different sections across the thickness of (a) $B/(W-a) = 1$, (b) $B/(W-a) = 0.5$, and (c) $B/(W-a) = 0.12$ CT specimens. | 132 |
| Figure 4.33 | The mean stress, σ_m , directly ahead of the crack-tip ($\theta = 0^\circ$) in four different sections across the thickness of (a) $B/(W-a) = 1$, (b) $B/(W-a) = 0.5$, and (c) $B/(W-a) = 0.12$ CT specimens. | 134 |
| Figure 4.34 | Distribution of cylindrical stresses around the corner point of the boundary layer formulations of an elastic perfectly-plastic ($n = \infty$) thin plate. | 136 |
| Figure 4.35 | Distribution of cylindrical stresses; (a) the hoop stress, $\sigma_{\theta\theta}$, (b) the radial stress, σ_{rr} , and (c) the shear stress, $\sigma_{r\theta}$, around the corner point of CT specimens of different thicknesses in non-hardening condition ($n = \infty$). | 138 |
| Figure 4.36 | Load versus load-line displacement (LLD) for the medium thickness and thin CT specimens. | 139 |
| Figure 4.37 | Values of J-integral measured following ASTM standard and obtained on the 5th and 26th contours of finite elements of the (a) $B/(W-a) = 0.5$, and (b) $B/(W-a) = 0.12$ CT specimens. | 141 |
| Figure 4.38 | Example of the (a) horizontal displacement, u_1 , and (b) vertical displacement, u_2 , fields in the vicinity of crack-tip in the medium thickness ($B/(W-a) = 0.5$) CT specimen at the maximum load (1 pixel = 11.2 μm). | 142 |
| Figure 4.39 | Example of the (a) vertical normal strain, ε_{22} , (b) lateral normal strain, ε_{11} , and (c) shear strain, ε_{12} , fields in the | 143 |

vicinity of crack-tip in the medium thickness ($B/(W-a) = 0.5$) CT specimen at the maximum load (1 pixel = 11.2 μm).

- Figure 4.40 Radial distribution of the vertical displacement, u_2 , at the free-surface of the medium thickness ($B/(W-a) = 0.5$) CT specimen at (a) $\theta = 45^\circ$, and (b) $\theta = 90^\circ$ obtained numerically and experimentally. 144
- Figure 4.41 Radial distribution of the horizontal displacement, u_1 , at the free-surface of the medium thickness ($B/(W-a) = 0.5$) CT specimen at (a) $\theta = 0^\circ$, (b) $\theta = 45^\circ$, and (c) $\theta = 90^\circ$ obtained numerically and experimentally. 145
- Figure 4.42 Radial distribution of the vertical displacement, u_2 , at the free-surface of the thin ($B/(W-a) = 0.12$) CT specimen at (a) $\theta = 45^\circ$, and (b) $\theta = 90^\circ$ obtained numerically and experimentally. 146
- Figure 4.43 Radial distribution of the horizontal displacement, u_1 , at the free-surface of the thin ($B/(W-a) = 0.12$) CT specimen at (a) $\theta = 0^\circ$, (b) $\theta = 45^\circ$, and (c) $\theta = 90^\circ$ obtained numerically and experimentally. 147
- Figure 4.44 Radial distribution of the vertical normal strain, ε_{22} , at the free-surface of the medium thickness ($B/(W-a) = 0.5$) CT specimen at (a) $\theta = 0^\circ$, (b) $\theta = 45^\circ$, and (c) $\theta = 90^\circ$ obtained numerically and experimentally. 149
- Figure 4.45 Radial distribution of the lateral normal strain, ε_{11} , at the free-surface of the medium thickness ($B/(W-a) = 0.5$) CT specimen at (a) $\theta = 0^\circ$, (b) $\theta = 45^\circ$, and (c) $\theta = 90^\circ$ obtained numerically and experimentally. 150
- Figure 4.46 Radial distribution of the in-plane shear strain, ε_{12} , at the free-surface of the medium thickness ($B/(W-a) = 0.5$) CT specimen at (a) $\theta = 0^\circ$, (b) $\theta = 45^\circ$, and (c) $\theta = 90^\circ$ obtained numerically and experimentally. 151
- Figure 4.47 Radial distribution of the vertical normal strain, ε_{22} , at the free-surface of the thin ($B/(W-a) = 0.12$) CT specimen at (a) $\theta = 0^\circ$, (b) $\theta = 45^\circ$, and (c) $\theta = 90^\circ$ obtained numerically and experimentally. 153

| | | |
|-------------|--|-----|
| Figure 4.48 | Radial distribution of the lateral normal strain, ε_{11} , at the free-surface of the thin ($B/(W-a) = 0.12$) CT specimen at (a) $\theta = 0^\circ$, (b) $\theta = 45^\circ$, and (c) $\theta = 90^\circ$ obtained numerically and experimentally. | 154 |
| Figure 4.49 | Radial distribution of the in-plane shear strain, ε_{12} , at the free-surface of the thin ($B/(W-a) = 0.12$) CT specimen at (a) $\theta = 0^\circ$, (b) $\theta = 45^\circ$, and (c) $\theta = 90^\circ$ obtained numerically and experimentally. | 155 |
| Figure 4.50 | Radial distribution of the equivalent plastic strain, ε_p , at the free-surface of (a) $B/(W-a) = 0.5$, and (b) $B/(W-a) = 0.12$ CT specimens at $\theta = 0^\circ, 45^\circ$, and 90° . | 156 |
| Figure 4.51 | Radial distribution of in-plane corner stresses directly ahead of the corner vertex ($\theta = 0^\circ$) in both medium thickness and thin CT specimens. | 158 |
| Figure 4.52 | The hoop stress as a function of $J/z\sigma_0$ at $\theta = 0^\circ$, at (a) $r = 2J/\sigma_0$, and (b) $r = 5J/\sigma_0$ for CT specimens of different thicknesses at four through-thickness section, $z/t = 0.032, 0.1, 0.2, 0.5$. | 160 |
| Figure 4.53 | The mean stress as a function of $J/z\sigma_0$ at $\theta = 0^\circ$, at (a) $r = 2J/\sigma_0$, and (b) $r = 5J/\sigma_0$ for CT specimens of different thicknesses at four through-thickness section, $z/t = 0.032, 0.1, 0.2, 0.5$. | 161 |
| Figure 4.54 | Exponential curves of out-of-plane constraint loss of $\sigma_{\theta\theta}$ at the distances (a) $r = 2J/\sigma_0$, and (b) $r = 5J/\sigma_0$, at angles in between 0° to 165° around the crack-tip of boundary layer formulations and CT models of different thicknesses. | 164 |
| Figure 4.55 | Variation of the sensitivity constant, γ , with respect to angle, θ , around the crack-tip. | 165 |
| Figure 4.56 | The hoop stress as a function of $J/z\sigma_0$ at $\theta = 45^\circ$, at (a) $r = 2J/\sigma_0$, and (b) $r = 5J/\sigma_0$ for CT specimens of different thicknesses at four through-thickness section, $z/t = 0.032, 0.1, 0.2, 0.5$. | 167 |

| | | |
|-------------|--|-----|
| Figure 4.57 | The mean stress as a function of $J/z\sigma_0$ at $\theta = 45^\circ$, at (a) $r = 2J/\sigma_0$, and (b) $r = 5J/\sigma_0$ for CT specimens of different thicknesses at four through-thickness section, $z/t = 0.032, 0.1, 0.2, 0.5$. | 168 |
| Figure 4.58 | The crack-tip dimensional length scales associated with semi-infinite three-dimensional boundary layer formulations. | 170 |
| Figure 4.59 | Exponentially decaying constraint loss. | 172 |
| Figure 4.60 | Variation of $\Delta\sigma$ along a crack front for $\gamma = 1, 2, 4, 6, \text{ and } 8$, at $\Omega_{far} = 8$. | 172 |
| Figure 4.61 | The transition of the three-dimensional stress fields from the familiar plane strain $\Delta\sigma = 1$ (a), to the plane stress $\Delta\sigma = 0$ (d) fields. | 176 |
| Figure 4.62 | The asymptotic stresses estimated using the proposed analytical solutions (in solid lines), and through finite element analysis (in dashed lines) for $\Delta\sigma = 0.98, 0.65, 0.26$. | 179 |
| Figure 4.63 | Through-thickness variation of normalized J_{loc} for $J_{far} = 100 \text{ N/mm}$ in a 25 mm CT specimen, estimated using Equation (4.1), and presented by Tkach and Burdekin (2012). | 181 |
| Figure 4.64 | Asymptotic hoop stress, $\sigma_{\theta\theta}$, in five different sections across the thickness for $\Delta\sigma = 0.99, 0.86, 0.76, 0.66, \text{ and } 0.56$. | 181 |
| Figure 4.65 | (a) Radial distribution of $\sigma_{\theta\theta}$, approximated using the proposed three-dimensional solution, and (b) radial distribution of σ_{22} reported by Tkach and Burdekin (2012). | 182 |

LIST OF ABBREVIATIONS

| | |
|-------|---|
| 2D | Two-dimensional |
| 3D | Three-dimensional |
| BLF | Boundary layer formulation |
| CCP | Center cracked tension panel |
| CMOD | Crack-mouth opening displacement |
| CT | Compact tension |
| CTOD | Crack-tip opening displacement |
| DE(T) | Double-edge-crack tension |
| DIC | Digital image correlation |
| DOF | Degree of freedom |
| EPFM | Elastic-plastic fracture mechanics |
| ESPI | Electronic speckle pattern interferometry |
| HPC | High performance computing |
| LEFM | Linear-elastic fracture mechanics |
| LGC | Large geometry change |
| LLD | Load line displacement |
| M(T) | Middle-crack tension |
| SE(B) | Single-edge-crack bending |
| SENB | Single edge notched bend bar |
| SGC | Small geometry change |

LIST OF SYMBOLS

| | |
|-----------|---|
| A_2 | Constraint parameter in the $J - A_2$ approach |
| A_p | Global constraint parameter in the $J - A_p$ approach |
| A_{pl} | Plastic area under load-displacement curve |
| a | Crack length |
| a_{eff} | Effective crack length |
| B | Specimen thickness |
| b_o | Initial blunted crack-tip notch |
| C | Correlation factor |
| c | Uncracked ligament size |
| E | Young's modulus |
| G | Shear modulus |
| h | Stress triaxiality parameter |
| I_n | Integration constant in HRR solutions |
| J | J -integral |
| J_{far} | Remotely applied J -integral |
| J_{loc} | Local J -integral along a crack front |
| J_{el} | Elastic component of J -integral |
| J_{pl} | Plastic component of J -integral |
| k | Yield stress in shear |
| K | Stress intensity factor |
| n | Strain hardening exponent |
| P | Applied load |

| | |
|------------------------------------|---|
| P_o | Plastic limit load |
| Q | Constraint parameter in the $J - Q$ approach |
| RF | Reaction force |
| r | Radial distance ahead of a crack-tip |
| r_p | Radius of Irwin plastic zone |
| r_y | Radius of plastic zone |
| $s_{ij}(i, j = r, \theta, z)$ | Deviatoric stress components in cylindrical coordinate system |
| t | Specimen thickness |
| T | T -stress |
| T_z | Plane strain parameter in $J - T_z$ approach |
| $u_i(i = 1, 2, 3)$ | Displacement components in Cartesian coordinate system |
| $\tilde{u}_i(i = 1, 2)$ | Dimensionless displacement functions for HRR solutions |
| ν | Poisson's ratio |
| V | Volume element |
| W | Specimen width |
| W_ϵ | Strain energy density |
| z | Distance measured from the free-surface of a specimen |
| σ_{22}^{far} | Remotely applied uni-axial stress |
| σ_f | Fracture stress |
| σ_o | Yield stress |
| $\sigma_{ij}(i, j = 1, 2, 3)$ | Stress component in Cartesian coordinate system |
| $\sigma_{ij}(i, j = r, \theta, z)$ | Stress component in cylindrical coordinate system |
| σ_m | Mean stress |

| | |
|--|--|
| $\bar{\sigma}$ | von Mises equivalent stress |
| σ_{kk} | Volumetric stress |
| $\tilde{\sigma}_{ij}(i, j = r, \theta,)$ | Dimensionless stress function for HRR solutions |
| $\varepsilon_{ij}(i, j = 1, 2, 3)$ | Strain component in Cartesian coordinate system |
| ε_o | Yield strain |
| ε_p | Equivalent plastic strain |
| $\tilde{\varepsilon}_{ij}(i, j = 1, 2)$ | Dimensionless strain function for HRR solutions |
| α | Measure of stress deviation from plane strain field |
| α_g | Global constraint parameter in the $J - \alpha_g$ approach |
| β | Stress biaxiality ratio |
| γ_s | Surface energy per unit area |
| γ_p | Plastic work per unit area of surface created |
| $\gamma_{(r,\theta)}$ | Sensitivity constant of constraint loss curve in $J - \Delta\sigma$ approach |
| μ | J -Dominance parameter |
| $\delta_{ij}(i, j = 1, 2)$ | Kronecker delta |
| δ_t | Crack-tip opening displacement |
| δ_m | Crack-mouth opening displacement |
| Ω_{far} | Dimensionless loading parameter related to J_{far} |
| ρ | Proximity to plane strain parameter |
| ϕ | Constraint parameter in the $J - \phi$ approach |
| ϕ_i | Maxwell stress function |
| $\Delta\sigma$ | Multiplier constant represents the change of stress |
| Γ | Arbitrary contour around a crack-tip |

PENGUKURAN ELASTIK-PLASTIK MEDAN TEGASAN DI HUJUNG RETAKAN TIGA DIMENSI

ABSTRAK

Penilaian integriti struktur yang konvensional dirumuskan berdasarkan kepada kaedah terikan satah dua-dimensi untuk memberikan satu anggaran kerosakan yang konservatif. Namun begitu, kaedah ini sering membawa kepada pembaikan dan penutupan sesebuah struktur yang tidak sepatutnya. Konservatisme ini telah dikurangkan melalui kaedah dua-parameter dua-dimensi $J - T/Q$. Walau bagaimanapun kaedah $J - T/Q$ ini tidak dapat mengukur kehilangan kekangan di dalam hujung retakan tiga-dimensi yang membawa kepada penghasilan teknik-teknik tiga-dimensi baru di dalam bidang mekanik retak. Di antara kaedah pengukuran yang telah dicadangkan, kaedah $J - \Delta\sigma$ mempunyai dasar utama kaedah $J - T/Q$ dan telah terbukti mampu mengukur kekangan dalam dan luar satah untuk geometri yang rendah dan tinggi kekangan melalui penggunaan parameter $J/z\sigma_o$. Walaupun kaedah $J - \Delta\sigma$ telah menetapkan satu ciri penting tentang medan hujung retakan tiga-dimensi, penggunaan parameter $J/z\sigma_o$ untuk keadaan retakan yang lain masih tidak lengkap. Oleh itu, penyelidikan ini adalah bertujuan untuk menilai lebih mendalam sifat kehilangan kekangan hujung retakan di dalam masalah retakan yang kompleks seperti hujung retakan yang tumpul, medan penjuru, dan perihalan tentang medan tegasan yang lengkap di sekeliling hujung retakan tiga-dimensi.

Medan hujung retakan tiga-dimensi yang bersifat elastik-plastik tulen, sama ada di dalam keadaan plastik skala kecil dan plastik penuh telah dikaji melalui kaedah formulasi lapisan sempadan (BLF) dan analisa penuh terhadap spesimen tegangan

padat (CT) dengan merujuk kepada penyelesaian dua-dimensi bagi membolehkan corak kehilangan kekangan dikenal pasti. Keputusan menunjukkan kekangan luar satah di dalam BLF dan CT hilang daripada keadaan terikan satah di satah tengah spesimen kepada keadaan tegasan satah di satah berdekatan dengan permukaan bebas spesimen. Parameter $J/z\sigma_o$ telah terbukti dapat menyatukan kehilangan kekangan luar satah dalam CT spesimen ke dalam satu lokus tunggal tanpa mengira beban yang dikenakan dan ketebalan spesimen tersebut. Corak kehilangan kekangan dari segi $J/z\sigma_o$ telah dikesan bergantung kepada sudut sekeliling hujung retakan. Berdasarkan kepada definisi lengkap $J/z\sigma_o$, penyelesaian analitikal untuk mengenalpasti tegasan hujung retakan tiga-dimensi telah dicadangkan, dan telah dibuktikan bersamaan dengan medan yang diperolehi daripada penyelesaian berangka. Medan penjurong yang bersifat elastis-plastik telah dikenal pasti melalui eksperimen dan kaedah berangka, dimana kedua-dua penyelesaian menunjukkan keputusan yang relatifnya serupa.

Oleh itu, dapat disimpulkan bahawa kaedah $J - \Delta\sigma$ adalah kaedah yang sesuai kerana ia dapat mengukur kesan kekangan dalam dan luar satah, dan memberikan penerangan lengkap mengenai medan hujung kekangan tiga-dimensi. Oleh kerana kaedah $J - \Delta\sigma$ berdasarkan kepada teori utama kaedah $J - T/Q$ sambil mengambil kira kedua-dua kesan kekangan dalam dan luar satah, ia dapat mengatasi kekurangan kaedah dua-parameter dua-dimensi tersebut, dan seterusnya mengurangkan aspek konservatisme berkaitan dengan dasar terikan satah, dan boleh digunakan secara terperinci bersama kod penilaian struktur yang sedia ada seperti R6, British Standard BS 7910, American Petroleum Institute Fitness-for-Service API 579, dan Structural Integrity Assessment Procedure for European Industry (SINTAP).

QUANTIFICATION OF THREE-DIMENSIONAL ELASTIC-PLASTIC CRACK-TIP STRESS FIELDS

ABSTRACT

Conventional structural integrity assessments are formulated based on plane strain fracture toughness to provide a conservative estimate of failure. However, such approach often leads to unnecessary repair and shutdown of structures. This conservatism has been minimized by the two-parameter fracture mechanics $J - T/Q$. However, the $J - T/Q$ approach is incapable of quantifying three-dimensional crack-tip constraint loss that leads to the emergence of new three-dimensional techniques in fracture mechanics. Amongst the quantification approaches that have been recently proposed, the $J - \Delta\sigma$ approach holds the key requirements of the $J - T/Q$ theory, and has been shown to be able to quantify the in-plane and out-of-plane constraint losses in high and low constraint geometries through the use of parameter $J/z\sigma_o$. Although the $J - \Delta\sigma$ approach has established an important feature of the three-dimensional crack-tip fields, the application of $J/z\sigma_o$ to other fracture conditions is still lacking. Therefore, this research is motivated to further assess the nature of crack-tip constraint loss in complex fracture problems such as blunted crack-tips, corner fields and description of complete stress fields around three-dimensional crack-tip.

The elastic perfectly-plastic three-dimensional crack-tip fields in contained yielding and full plasticity conditions have been respectively examined through the means of boundary layer formulations (BLF), and a full-field analysis of compact tension (CT) specimens, with reference to limiting two-dimensional solutions to allow the pattern of constraint loss to be recognized. The results show that the out-of-plane

constraint in BLF and CT models is lost from a plane strain condition at the midplane to a plane stress field near the free-surface. The parameter $J/z\sigma_o$ has been shown to be able to unify the out-of-plane constraint loss in CT specimens into a single curve regardless of load and specimen thickness. The nature of constraint loss in term of $J/z\sigma_o$ has been observed to be dependent on the angle around the crack-tip. Based on the complete definition of $J/z\sigma_o$, analytical solutions for three-dimensional crack-tip stress fields have been developed, which appear to be in good agreement with the numerically-predicted crack-tip fields. The elastic-plastic corner fields have been characterized numerically and experimentally, wherein both solutions are shown to be relatively comparable.

Therefore, it can be concluded that the $J - \Delta\sigma$ approach is an appropriate approach as it is capable of quantifying the effect of in-plane and out-of-plane constraints, and providing a complete description of three-dimensional crack-tip fields. As the $J - \Delta\sigma$ approach adopts the key requirements of the $J - T/Q$ theory while taking account both in-plane and out-of-plane constraint effects, it addresses the limitation of the two-parameter approach, and thus further reduces the conservatism aspect of the plane strain framework, and can be usefully integrated into the existing structural integrity assessment codes such as the R6, the British Standard BS 7910, the American Petroleum Institute Fitness-for-Service API 579 and the Structural Integrity Assessment Procedure for European Industry (SINTAP).

CHAPTER ONE

INTRODUCTION

1.1 Background

Engineering and industrial structures such as pressure vessels, power plants, and offshore platforms may contain defects including cracks and corruptions that can occur during manufacture and service life. The integrity of these structures is crucial to ensure a safe, economic, and sustained operation. The procedure for the integrity assessment of structures containing defects has been developed based on fracture mechanics principles and standardized in codes including the UK nuclear industry's fracture assessment code R6 (R6, 2001), the British Standard, BS 7910 (BSi, 2005), the American Petroleum Institute Fitness-for-Service, API 579 (API, 2000), and the Structural Integrity Assessment Procedures for European Industry, SINTAP (SINTAP, 1999). The assessment codes enable operators and fabricators to make assertive decisions on the most appropriate remedial measures to take during design, fabrication and operation in ensuring the safety of their structures.

Despite the substantial benefits offered by the application of the fracture assessment methods, the codes have been claimed to be too conservative as they are primarily based on conservative variables such as lower bound values of resistance to fracture or plane strain fracture toughness that is exhibited in thick specimens and parameterized by single parameter K , J , and CTOD. However, it is well known that the toughness of a cracked body varies over a range of thicknesses, and the single parameter fracture mechanics does not consider the enhanced fracture toughness due to the in-plane and the out-of-plane constraint losses that occur in actual three-

dimensional structures. Consequently, the conservative aspect of the structural integrity assessment may cause premature defects to be considered dangerous and leads to the unnecessary maintenance and shutdown of structures and plants.

The conservatism associated with two-dimensional plane strain approach has been reduced through the implementation of the two-parameter fracture mechanics $K/J - T$ (Betegón & Hancock, 1991), and $J - Q$ (O'Dowd & Shih, 1991). The first parameter quantifies the crack-tip deformation while the second parameter measures the level of crack-tip constraint. Although the application of two-parameter fracture mechanics to full-field three-dimensional solutions has been increasingly made, it is restricted to the in-plane geometry effects in thick specimen to the neglect of out-of-plane or thickness effects (Kim et al., 2001; Yuan et al., 1995). It was argued that the two-parameter approaches are relevant only when the out-of-plane constraint is bounded (O'Dowd, 1995; Pardoen et al., 1999) that leads to the conclusion that a parameter based on plane strain cannot fully describe the out-of-plane constraint loss (Yuan & Brocks, 1998).

Consequently, quantification of the out-of-plane constraint effect in three-dimensional cracked bodies has become central to fracture mechanics. Newman et al. (1993) proposed constraint parameter, α_g , but it was dependent on geometry and not unique. In a separate development, a plane strain parameter, T_z , was proposed to describe the three-dimensionality of crack-tip fields (W. Guo, 1993a), but the application of T_z is limited only to geometries with positive T -stress and a small range of material responses. Yusof (2006) proposed a modified $J - Q$ approach with a unified deformation parameter, $J/z\sigma_o$, which is called the $J - \Delta\sigma$ approach, but his work was limited in the application of the approach to a wider range of crack

configurations. Mostafavi et al. (2010) and J. Yang et al. (2013) individually introduced a constraint parameter with a similar concept that was based on semi-empirical measures, yet the application of the parameters is restricted to the conditions proposed in their work only.

1.2 Problem Statement

The quantification of the three-dimensionality of elastic-plastic crack-tip fields for the purposes of minimizing the conservatism of two-dimensional plane strain approach is still inconclusive as the quantification approaches that have been proposed have specific limitations with regards to their applicability and credibility.

Although both $J - T_z$ and $J - \Delta\sigma$ approaches were based on the analysis of the state of crack-tip stresses, Leong (2017) profoundly demonstrated that the $J - T_z$ approach was only valid for high constraint geometries with strain hardening exponent, $n \leq 13$. On the other hand, Leong (2017) showed that the $J - \Delta\sigma$ approach can be extended to describe strain hardening three-dimensional crack-tip fields in deep and shallow cracked of both high constraint (SENB) and low constraint (CCP) geometries. On top of providing the unified measure of constraint loss, the $J - \Delta\sigma$ approach was claimed to be more advantageous over the $J - T_z$ in a way that it eliminates the needs to determine the T_z distribution in the respective cracked geometry. As the $J - \Delta\sigma$ approach closely holds the key requirements of the $J - T/Q$ theory while taking account the in-plane and out-of-plane constraints effect, the limitation of the two-parameter fracture mechanics and the conservatism of the plane strain approach can be addressed. For this reason and its advantageous over $J - T_z$, the $J - \Delta\sigma$ approach is further evaluated in this study through a quantification of constraint loss in deeply cracked CT specimens.

Since the derivation of the $J - \Delta\sigma$ approach was based on the three-dimensionality of crack-tip stress fields with the influence of out-of-plane constraint variations, the approach is believed to be potentially capable of providing a complete description of three-dimensional crack-tip fields in all types of cracked bodies. Although the $J - \Delta\sigma$ approach has established an important feature of the three-dimensional crack-tip fields, the limit of application of the parameter $J/z\sigma_o$ is still not completely examined. For instance, the $J - \Delta\sigma$ approach through the parameter $J/z\sigma_o$ only looks at the constraint loss directly ahead of the crack front ($\theta = 0^\circ$), and leaves those at the larger angles around the crack-tip undetermined that have yet to be resolved. Therefore, this research is motivated to further assess the nature of crack-tip constraint loss in complex fracture problems such as blunted crack-tips, corner fields and description of complete stress fields around three-dimensional crack-tip.

1.3 Objectives of Research

The objectives of the present study are as follow:

- a) To characterize the nature of elastic perfectly-plastic three-dimensional crack-tip border fields in three-dimensional boundary layer formulations (BLF) of small geometry change (SGC) and large geometry change (LGC) models, and in full-field compact tension (CT) specimen models.
- b) To characterize the structure of elastic-plastic corner displacement and strain fields using an experimental optical mechanics approach.
- c) To evaluate the $J - \Delta\sigma$ approach through a quantification of constraint loss in deeply cracked CT specimens.
- d) To establish the nature of constraint loss at all angles around the crack-tip following the $J - \Delta\sigma$ approach.

- e) To quantify the stress state of three-dimensional crack-tip fields as a function of load and geometry using the $J - \Delta\sigma$ analytical framework.

1.4 Scope of Research Work

The overall scope of the present research is diagrammatically outlined in Figure 1.1, which focuses on the characterization of the nature of three-dimensional crack-tip fields in an elastic perfectly-plastic condition with the influence of out-of-plane constraint.

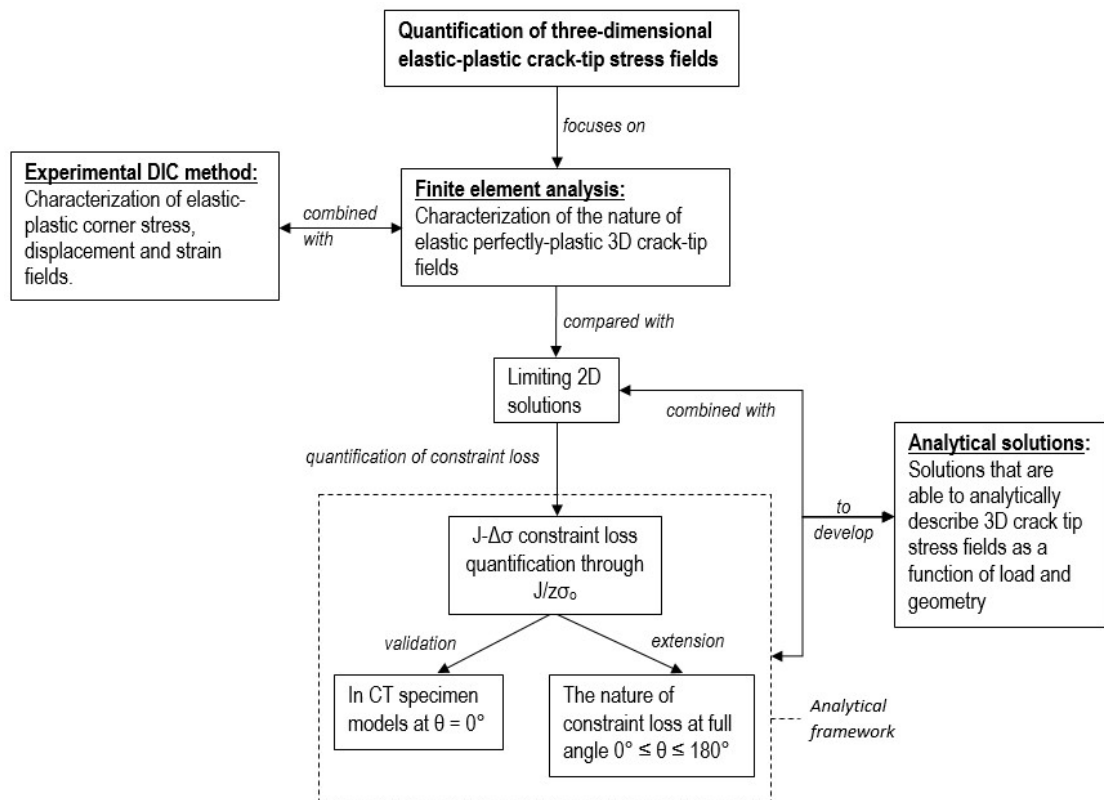


Figure 1.1: The overall scope of the current research work.

The through-thickness variations of the three-dimensional crack-tip stress fields are assessed with reference to the limiting two-dimensional plane strain and plane stress solutions to examine the transition of crack-tip stress state from the centre of the plate (midplane) to the free-surface, and thus allowing the pattern of constraint loss to be recognized. The out-of-plane constraint loss directly ahead of the crack front ($\theta = 0^\circ$) in CT specimen models is quantified using the $J - \Delta\sigma$ approach through the unified deformation parameter $J/z\sigma_o$, which is then used to further characterize the nature of out-of-plane constraint loss on at full angle $0^\circ \leq \theta \leq 180^\circ$ around the crack-tip. The complete quantification of the crack-tip constraint loss through the $J - \Delta\sigma$ approach and the parameter $J/z\sigma_o$ provides analytical framework for describing the stress state of three-dimensional crack-tip fields as a function of load and geometry. This is executed mainly through a proposed multiplier factor, $\Delta\sigma$, which is a function of the parameter $J/z\sigma_o$, that essentially governs the transition of stress state through the thickness, from a plane strain condition at the midplane, to a plane stress field near the free-surface.

The characterization of an elastic-plastic corner field is based on experimental and numerical analyses of CT specimens subjected to a tensile loading. Due to experimental limitations, such as the load range of the universal testing machine available in the laboratory, only $B/(W - a) = 0.5$, and $B/(W - a) = 0.12$ CT specimens are considered for this task. The near-tip displacement and strain fields are acquired and analysed using a digital image correlation (DIC) method through a commercially available image correlation software, DaVis. The calculated displacement and strain fields are compared with the numerically-predicted fields for assessment and validation purposes.

1.5 Thesis Outline

This thesis contains five chapters. Following the current introduction, the relevant literatures are reviewed in Chapter 2 that covers two related subjects in fracture mechanics, starting off with the topic of analytical fracture mechanics, and followed by the topic of experimental fracture mechanics. Chapter 3 describes the numerical techniques used. to construct three-dimensional finite element models of cracked specimens, and experimental procedures performed for the corner field characterization. The results of the study are presented and discussed in Chapter 4, where the nature of the elastic perfectly-plastic three-dimensional border crack-tip stress field of BLF and CT specimen are analysed with respect to out-of-plane constraint loss. The development of analytical solutions for three-dimensional crack-tip stress fields is presented at the end of this chapter. Finally, the concluding remarks of the studies and the recommendations for future works are conveyed in Chapter 5.

CHAPTER TWO

LITERATURE REVIEW

This chapter begins with a review of the analytical fracture mechanics, evolving from the fundamental topic of two-dimensional crack-tip field, to the progressive topic of three-dimensional crack-tip field, which includes the discussion on the limitation of single-parameter and two-parameter fracture mechanics in describing three-dimensional crack-tip constraint that leads to a continuous development of parametric quantifications of the constraint effects. The distinctive characteristics of a corner field, which remain an open question, are reviewed separately in the following subsection. A brief introduction to the methods of experimental fracture mechanics, ranging from the most classical strain gauge to most advanced digital image correlation (DIC) method. A detailed description of the fundamental concepts of DIC is given in the subsequent subsection.

2.1 Analytical Fracture Mechanics

Fracture mechanics was developed to understand the correlation of microscopic fracture behaviour in different cracked structures through some kind of a measurable parameters. The correlation, such as the initiation of crack growth was based upon the similitude of near crack-tip stress and deformation fields (Irwin, 1957). The crack-tip fields were conventionally represented by a prevailing singular crack-tip fields, which were characterized by a single parameter, such as the stress intensity factor K of a linear elastic fracture mechanics (LEFM) and J -integral of an elastic-plastic fracture mechanics (EPFM) approaches. Figure 2.1 shows the chronological

development of fracture mechanics concept in continuum mechanics based on seminal works that are reviewed in the following sections.

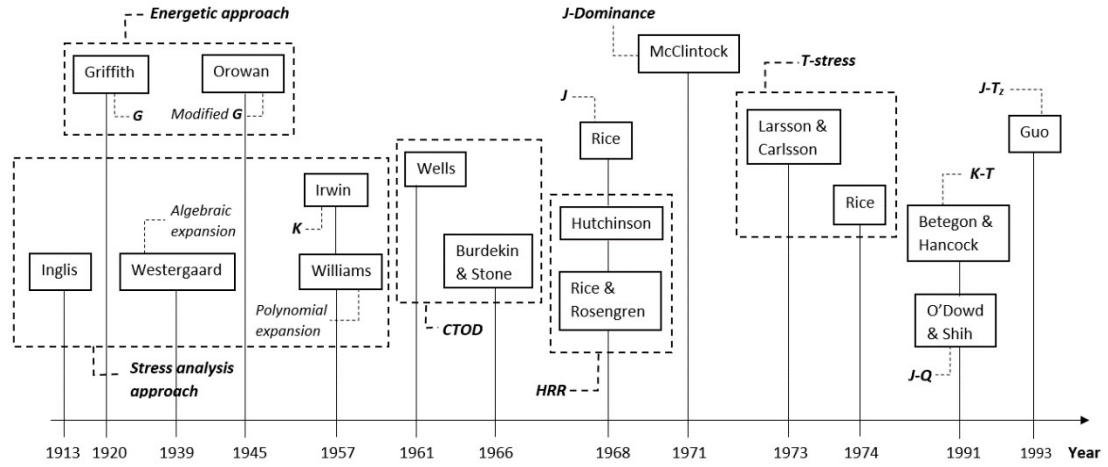


Figure 2.1: Seminal works in the development of fracture mechanics concept in continuum mechanics.

2.1.1 Two-Dimensional Crack-tip Fields

The traditional theory of fracture mechanics began with the Inglis analysis (Inglis, 1913) of an elliptical hole in a uniformly stressed plate (Figure 2.2) that provided the first analytical description of the effect of stress concentration around geometric singularities in a structure. Using complex potential to satisfy the boundary problem, Inglis expressed the opening stress at the edge of the major axes as:

$$\sigma_{22} = \sigma_{22}^{far} \left(1 + 2\frac{a}{b}\right) = \sigma_{22}^{far} \left(1 + 2\sqrt{\frac{a}{\rho}}\right) \quad (2.1)$$

where σ_{22}^{far} is the remotely applied uni-axial stress, a is the semi major-axis of the ellipse, b is the semi-minor axis, and $\rho = b^2/a$ is the radius of the curvature at the end of the semi-major axis. The Inglis solution predicts an infinite stress at the tip in the limit of an ideally sharp crack as ρ approaches zero. This anomaly led to the

development of a theoretical analysis of fracture based on energy rather than local stress.

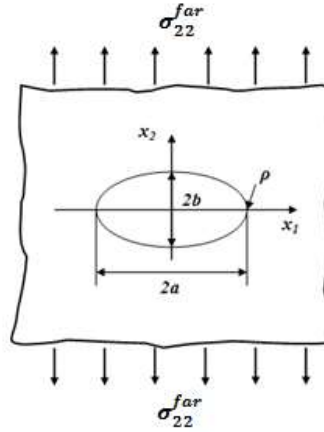


Figure 2.2: Elliptical hole in an infinite plate.

In response to the paradox of the infinite stress at a crack-tip of a sharp crack, Griffith (1920) developed a crack propagation theory based on a basic energy balance that was for a crack to grow, the net potential energy of a system must be sufficient to overcome the surface energy of the material. By using the Griffith energy balance for an increment of crack extension as well as adopting the Inglis solution, Griffith solved for the fracture stress, σ_f in a cracked plate as:

$$\sigma_f = \left(\frac{2E\gamma_s}{\pi a} \right)^{1/2} \quad (2.2)$$

where E is the modulus of elasticity, and γ_s is the surface energy of the material.

The Griffith criterion suitably predicted the relationship between strength and crack size in brittle materials, but fails when applied to ductile materials due to not being able to take into account the plastic energy developed at the crack-tip sufficiently. Aimed at extending its applicability, Orowan (1945) modified the Griffith expression

by including a term describing the energy dissipated by local plastic flow. The revised expression is given by:

$$\sigma_f = \left(\frac{2E(\gamma_p + \gamma_s)}{\pi a} \right)^{1/2} \quad (2.3)$$

where γ_p is the plastic work per unit area of surface created, which was experimentally found to be much larger than γ_s , indicating the domination of crack-tip plasticity in fracture process even in highly brittle materials.

The next major development in fracture mechanics was revolved around the nature of the asymptotic elastic crack-tip field established by Westergaard (1939) and Williams (1957). According to the algebraic expansion of Westergaard, the stress field for a central crack in an infinite plate can be given using Cartesian stresses and cylindrical coordinates centred at the crack-tip as defined in Figure 2.3.

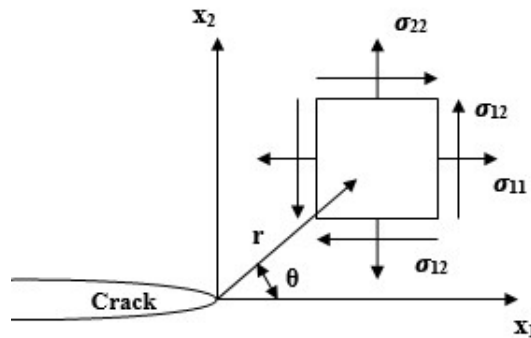


Figure 2.3: Coordinate axis ahead of a crack-tip used in Westergaard asymptotic solution.

The Westergaard plane strain stress field was defined as:

$$\sigma_{11} = \frac{\sigma\sqrt{a}}{\sqrt{2r}} \cos \frac{\theta}{2} \left(1 + \cos \frac{\theta}{2} \sin \frac{3\theta}{2} \right) \quad (2.4a)$$

$$\sigma_{22} = \frac{\sigma\sqrt{a}}{\sqrt{2r}} \cos \frac{\theta}{2} \left(1 - \cos \frac{\theta}{2} \sin \frac{3\theta}{2} \right) \quad (r \ll a) \quad (2.4b)$$

$$\sigma_{12} = \frac{\sigma\sqrt{a}}{\sqrt{2r}} \sin \frac{\theta}{2} \cos \frac{\theta}{2} \cos \frac{3\theta}{2} \quad (2.4c)$$

Here a is the half crack length. Irwin (1957) expressed the Westergaard equations in a generalized form:

$$\sigma_{ij}^{(\alpha)}(r, \theta) = \frac{K_{\alpha}}{\sqrt{2\pi r}} f_{ij}^{(\alpha)}(\theta) \quad (2.5)$$

where $f_{ij}^{(\alpha)}(\theta)$ is a geometrical factor, and $\alpha = I, II, III$ defines the three possible modes of crack opening as illustrated in Figure 2.4. The parameter K_{α} is called the stress intensity factor as a measure of crack-tip singularity. For a crack in an infinite plate, K is given by:

$$K = \sigma^{far} \sqrt{\pi a} \quad (2.6)$$

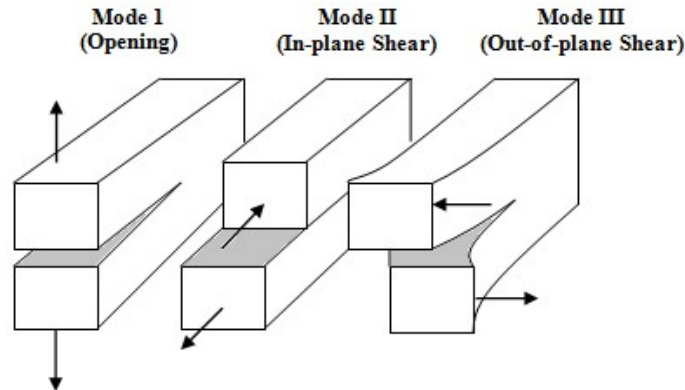


Figure 2.4: Three modes of deformation.

For the Mode-I crack opening, the singular stress field and associated displacement field ahead of a crack-tip in an isotropic linear elastic material can be obtained using the following equations by Rice (1968a):

$$\begin{Bmatrix} \sigma_{11} \\ \sigma_{12} \\ \sigma_{22} \end{Bmatrix} = \frac{K_I}{\sqrt{2\pi r}} \cos\left(\frac{\theta}{2}\right) \begin{Bmatrix} 1 - \sin(\theta/2)\sin(3\theta/2) \\ \sin(\theta/2)\cos(3\theta/2) \\ 1 + \sin(\theta/2)\sin(3\theta/2) \end{Bmatrix} \quad (2.7)$$

$$\begin{Bmatrix} u_1 \\ u_2 \end{Bmatrix} = \frac{K_I}{2G} \sqrt{\frac{r}{2\pi}} \begin{Bmatrix} \cos(\theta/2)[\kappa - 1 + 2\sin^2(\theta/2)] \\ \sin(\theta/2)[\kappa + 1 - 2\sin^2(\theta/2)] \end{Bmatrix} \quad (2.8)$$

where shear modulus, $G = E/2(1 + \nu)$, and $\kappa = 3 - 4\nu$ for plane strain, while $\kappa = (3 - \nu)/(1 + \nu)$ for generalized plane stress.

Fracture mechanics approach to crack-tip plasticity begins with simple corrections to the linear elastic solution proposed by Irwin (1960) and Dugdale (1960). Irwin suggested that plasticity causes the crack to behave as if it were slightly longer than its true physical length so that the effective crack length, a_{eff} can be considered as an inclusion of the plastic zone correction to the length of the crack:

$$a_{eff} = a + r_y \quad (2.8)$$

where a is half crack length, and r_y is the radius of plastic zone as in Figure 2.5. The plastic zone correction of Irwin, r_p is given by:

$$r_p = \frac{1}{\pi} \left(\frac{K_I}{\sigma_o} \right)^2 \quad (2.9)$$

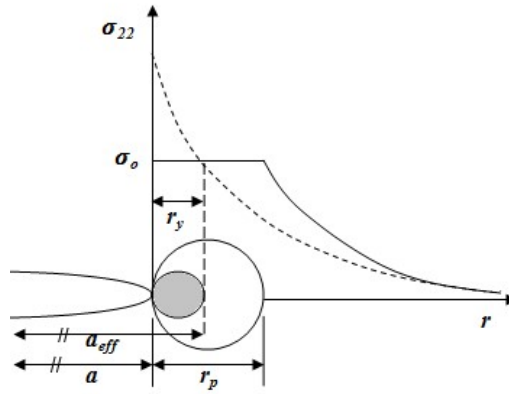


Figure 2.5: Irwin plastic zone correction.

Subsequently, Dugdale's plastic zone correction was formulated using a strip-yield model, which assumes that plasticity concentrates in a strip ahead of the crack, as shown in Figure 2.6.

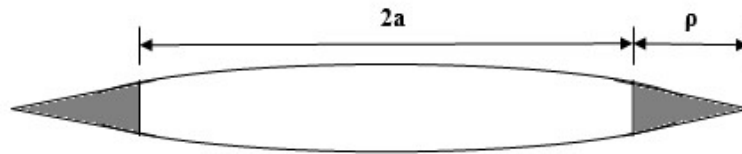


Figure 2.6: Dugdale's strip yield plastic zones.

Based on the requirement that the stresses in the elastic region outside the plastic zone must be finite, the Dugdale's plastic zone, ρ is:

$$\rho = \frac{\pi}{8} \left(\frac{K_I}{\sigma_o} \right)^2 \quad (2.10)$$

As $1/\pi \approx \pi/8$, it could be deduced that the Irwin and strip-yield corrections estimate somewhat similar plastic zone sizes.

Wells (1961) noticed that large plastic deformation caused an initially sharp crack-tip to blunt to a finite radius that moves the crack faces apart. He claimed that the degree of crack blunting at fracture increases with the toughness of the material. Based on these observations, Wells (1961) proposed an alternative fracture toughness parameter using the displacement of the crack faces, denoted the crack-tip opening displacement or CTOD, δ_t .

Experimentally, the CTOD can be determined through the crack mouth opening displacement CMOD, δ_m by measuring the surface displacement across the crack front, as shown in Figure 2.7(a). Shih (1981) suggested that the CTOD should be defined by the displacement at the intersection of a 90° vertex with the crack flanks, as illustrated in Figure 2.7(b).

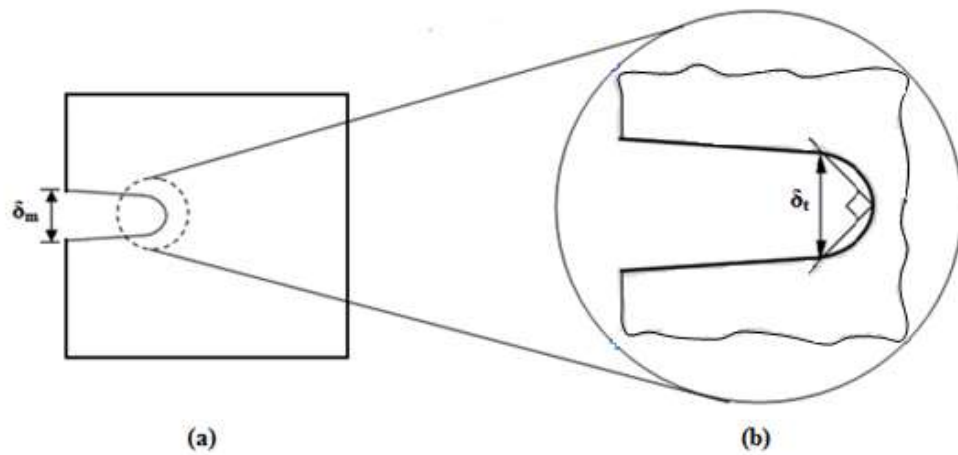


Figure 2.7: The crack-tip opening displacement measured from (a) crack mouth opening displacement, and (b) at the intersection of 90° vertex with the crack flanks.

Using the Dugdale strip yield model, Burdekin and Stone (1966) expressed the relationship between CTOD and the applied stress as:

$$\delta_t = \frac{8\sigma_o a}{\pi E} \ln \sec \left[\frac{\pi \sigma}{2 \sigma_o} \right] \quad (2.11)$$

The (ln sec) series expansion gives:

$$\begin{aligned} \delta_t &= \frac{8\sigma_o a}{\pi E} \left[\frac{1}{2} \left(\frac{\pi \sigma}{2 \sigma_o} \right)^2 + \frac{1}{12} \left(\frac{\pi \sigma}{2 \sigma_o} \right)^4 + \dots \right] \\ &= \frac{K_I^2}{E\sigma_o} \left[1 + \frac{1}{6} \left(\frac{\pi \sigma}{2 \sigma_o} \right)^2 + \dots \right] \end{aligned} \quad (2.12)$$

At very small values of σ/σ_o Equation (2.12) reduces to the small scale yielding relationship:

$$\delta_t = \frac{\sigma^2 \pi a}{E\sigma_o} = \frac{K_I^2}{E\sigma_o} \frac{1}{m} = \frac{G}{\sigma_o} \frac{1}{m} \quad (2.13)$$

where the dimensionless constant m is included to differentiate plane stress ($m = 1$) and plane strain ($m = 2$).

In 1968, Rice (Rice, 1968b) developed a parameter, called J -integral, to characterize the crack-tip field of non-linear material by expressing the energy release rate as a line integral evaluated along an arbitrary contour around the crack-tip. The path independent J for any contour Γ (Figure 2.8) in anti-clockwise direction is defined as:

$$J = \int_{\Gamma} \left(W_{\varepsilon} dx_2 - \mathbf{T} \frac{\partial u}{\partial x_1} ds \right) \quad (2.14)$$

where the first term, W_ε is strain energy density, and the second term is the work done by the external forces where \mathbf{T} is the traction vector, \mathbf{u} is the displacement vector, and ds is an increment along the path Γ .

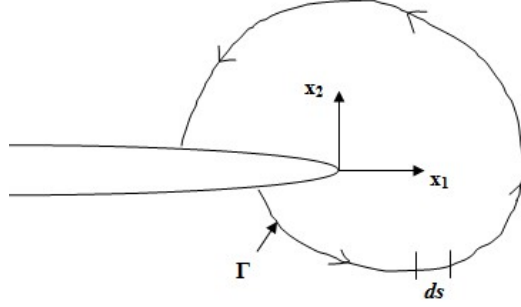


Figure 2.8: Arbitrary contour around a crack-tip.

Thus, J -integral was essentially equal to the energy release rate on a nonlinear elastic body containing a crack per unit fracture surface area.

Progress in understanding the elastic-plastic stress states began with asymptotic analysis of the crack-tip field. Hutchinson (1968b), and Rice and Rosengren (1968) independently derived an asymptotic series to characterize the crack-tip field in non-linear elasticity with power-law behavior, which was referred as the HRR field. The leading terms of the HRR stress, strain, and displacement fields are of the form:

$$\sigma_{ij} = \sigma_o \left(\frac{EJ}{\alpha\sigma_o^2 I_n r} \right)^{\frac{1}{n+1}} \tilde{\sigma}_{ij}(n, \theta); \quad (2.15a)$$

$$\varepsilon_{ij} = \frac{\alpha\sigma_o}{E} \left(\frac{EJ}{\alpha\sigma_o^2 I_n r} \right)^{\frac{n}{n+1}} \tilde{\varepsilon}_{ij}(n, \theta); \quad (2.15b)$$

$$u_i = \alpha\varepsilon_o r \left(\frac{J}{\alpha\sigma_o^2 I_n r} \right)^{\frac{n}{1+n}} \tilde{u}_i(n, \theta) \quad (i = 1, 2) \quad (2.15c)$$

where I_n is an integration constant that depends on the strain hardening exponent n , and the state of stress. The functions $\tilde{\sigma}_{ij}$, $\tilde{\varepsilon}_{ij}$, and \tilde{u}_i are the dimensionless angular functions tabulated by Shih (1983). Here J determines the magnitude of the HRR singularity fields in the same way the K characterizes the elastic crack-tip field.

In full plasticity, neither the asymptotic plastic field, nor the embedded local crack-tip blunting field were unique but were functions of the geometry and loading configurations. The conditions under which crack-tip fields correspond to the small scale yielding conditions, as characterised by J were referred to as the conditions for J -dominance (McClintock, 1971).

The limitations of J -dominance, or single parameter characterization of the crack-tip field were demonstrated by McClintock (1971) using the slip line analysis. From the analysis, McClintock (1971) showed that centre cracked panels were incapable of maintaining the crack-tip triaxiality with the hoop stress, $\sigma_{\theta\theta}$, of only $\frac{2}{\sqrt{3}}\sigma_o$. Figure 2.9 shows the different forms of slip line field for centre cracked and double edge cracked in tension. For a deeply cracked plate in bending, $\sigma_{\theta\theta}$ at the bending crack-tip was found to be approximately $2.5\sigma_o$.

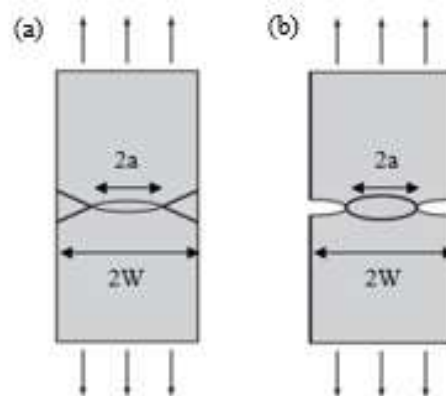


Figure 2.9: The slip line fields for (a) centre crack in tension, (b) double edge crack in tension.

The J -dominance limitations have been examined in detail by McMeeking and Parks (1979) who used finite element analysis to compare local blunting fields for edge cracked bend bars and centre crack tension panel in full plasticity with the corresponding small scale yielding solutions. Aiming to develop size requirements for specimens to retain the crack-tip triaxiality corresponding to small scale yielding, they argued that single parameter characterization can be maintained under condition that depends on the ligament size, c , which is expressed through a dimensionless factor, μ :

$$\mu = \frac{c\sigma_o}{J} \quad (2.16)$$

where $c = (W - a)$.

A major result of their work was the demonstration in fully plastic bend specimens of unique fields in the blunted crack-tip region, when scaled by J/σ_o . The stress distribution ahead of the blunting crack-tip in the edge cracked bend specimen at J values as large as $c\sigma_o/25$ was observed to be nearly identical to that of small scale yielding, suggesting that the minimum ligament size of $25J/\sigma_o$ is required to reasonably assure J -dominance of the crack-tip region in bend specimens. Due to their similar fully plastic flow fields, this requirement was presumed to apply to compact tension and three-point bend specimens as well (McMeeking & Parks, 1979). For centre cracked panel loaded in tension, however, a conservative estimate of $c = 200J/\sigma_o$ as a size limitation was proposed to assure the validity of J -characterized crack-tip fields. By repeating the work of McMeeking and Parks (1979) and comparing the full field solutions with small strain formulations, Shih and German (1981) later confirmed these requirements for maintaining J -dominance.

The geometry and loading dependence in plastic-dominated deformation is associated with the change in the level of hydrostatic or mean stress in the crack-tip field (McClintock, 1971). This is referred as the constraint level or the crack-tip triaxiality. The effect of in-plane geometry, e.g. crack length, can be quantified by the two-parameter fracture mechanics, which is primarily based on state of T -stress.

2.1.1(a) T -stress

Williams (1957) formulated an asymptotic polynomial expansion for the crack-tip stress field in an elastic infinite plate as:

$$\sigma_{ij}(r, \theta) = a_1(\theta)r^{-1/2} + a_2(\theta)r^0 + a_3(\theta)r^{1/2} + \dots \quad (2.17)$$

where $a_i (i = 1, 2, 3 \dots)$ are the angular functions and r is the radial distance from a crack-tip. The first term of the expansion corresponds to the Westergaard stress fields (Equation (2.4)) with a similar singularity of $1/\sqrt{r}$ that becomes infinite at the crack-tip. the second term corresponds to the stress acting parallel to the crack flanks, σ_{11} , and denoted as T -stress (Rice, 1974).

Neglecting the higher order terms, the asymptotic linear elastic stress field can be generalized as:

$$\sigma_{ij}(r, \theta) = \frac{K_I}{\sqrt{2\pi r}} f_{ij}(\theta) + T \delta_{1j} \delta_{i1} \quad (2.18)$$

Leevers and Radon (1982) claimed that T -stress can be related to K by a parameter known as stress biaxiality ratio, β :

$$\beta = \frac{T\sqrt{\pi A}}{K} \quad (2.19)$$

The magnitude of T -stress, which was expressed in terms of β , or T -stress concentration factor, T/σ_o , had been calculated using various methods and tabulated for a number of crack configurations. It has been noted that the T -stress was strongly dependent on crack geometries and loading type (Kfouri, 1986; Leever & Radon, 1982; Sham, 1991; Wang & Parks, 1992), and has a major effect on the stress level as well as the size and shape of the plastic zone ahead of the crack-tip (Larsson & Carlsson, 1973). Du and Hancock (1991) showed that negative T -stress enlarged the maximum radius of the plastic zone, while positive T -stress caused the plastic zone to decrease in size. The effect of T -stress on a large geometry change deformation field within $2\delta_t$ has been discussed by Bilby et al. (1986). Negative T -stresses were shown to reduce the maximum level of hydrostatic stress ahead of the crack, and thus enhancing ductility due to the loss of crack-tip triaxiality, which is in line with the experimental observations of Hancock and Cowling (1980). An extensive review of T -stress development and application was given in Gupta et al. (2015).

As T -stress acts parallel to the crack flanks and independent of the radial distance from the crack-tip, it has no effect on the J -integral. Therefore, in the cases of non-zero T -stress, the J characterization of stress field would be insufficient. Although these findings had been acknowledged for years (Bilby et al., 1986; Hancock & Cowling, 1980; Kfouri, 1986; Larsson & Carlsson, 1973; Leever & Radon, 1982), it was not until around 1990 that a great interest in quantifying the constraint effect on the crack-tip stress fields was shown. Amongst the approach proposed, the $K/J - T$, $J - Q$, and $J - A_2$ formulations were the three frameworks to receive the most attention in what has come to be known as two-parameter fracture mechanics. These three approaches are individually described in the following sections.

2.1.1(b) $K/J - T$ Approach

Hancock and co-workers (Al-Ani & Hancock, 1991; Betegón & Hancock, 1991; Du & Hancock, 1991) found that the T -stress may be a useful constraint parameter in quantifying the deviation of stress fields from HRR fields, and thus proposed the $K/J - T$ crack-tip stress estimation approach. Du and Hancock (1991) showed that the T -stress controlled the angular span of the constant stress region in the slip line field around the crack-tip in an elastic-perfectly plastic material, which is the source to the build-up of hydrostatic stress ahead of the crack-tip. Betegón and Hancock (1991) observed that the opening stress ahead of crack in strain hardening materials was reduced by an amount that depends only on the T -stress and is independent of the radial distance from the tip. As illustrated in Figure 2.10, the geometries with zero and positive T -stress cause the stress field to approach the HRR field, while geometries with a negative T -stress cause the opening stress ahead of the crack-tip to drop significantly.

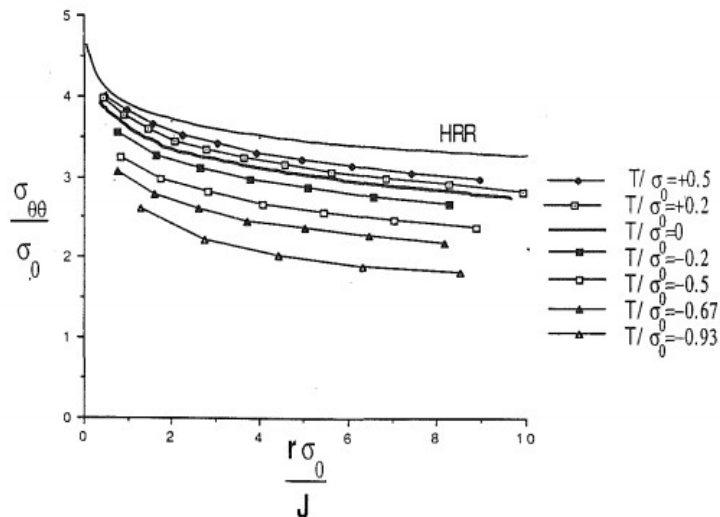


Figure 2.10: The hoop stress directly ahead of the crack-tip in boundary layer formulations as a function of T/σ_0 after Betegón and Hancock (1991).

Based on these observations, Betegón and Hancock (1991) proposed a two-parameter characterization of T -stress dependent on the stress fields, which is of the form:

$$\sigma_{\theta\theta}(r, T) = \sigma_{\theta\theta}(r, T = 0) + C(T, n) \quad (2.20)$$

where C is a constant which depends on the T -stress and the strain hardening exponent, n .

The $J - T$ two-parameter characterization of crack-tip stress fields thus unifies the problem of J -dominance in different geometries. Geometries that show positive T -stress can be described by the HRR field and characterized by J alone. Geometries with negative T -stress lose J -dominance, and therefore can be characterized by two-parameters, J and T , in a way that J scales the applied load, while T quantifies the constraint loss (Parks, 1992).

2.1.1(c) $J - Q$ Approach

O'Dowd and Shih (1991) argued that the applicability of the $K/J - T$ approach was essentially limited to the condition of small scale yielding and unable to characterize crack-tip fields into large plasticity. O'Dowd and Shih (1991), hence, introduced a consequential approach to the two-parameter known as the $J - Q$ approach. Based on the works by Li and Wang (1986) and Sharma and Aravas (1991), O'Dowd and Shih (1991) proposed that the crack-tip stress fields can be expressed in a two-term expansion of the form:

$$\sigma_{ij} = \sigma_{ij}^{HRR} + \sigma_o Q \left(\frac{r\sigma_o}{J} \right)^q \tilde{\sigma}_{ij} \quad (2.21)$$

where the notation Q is a hydrostatic stress parameter that represents the amplitude of the second term in the expansion. It was proposed that the exponent q can be approximated to zero if the stress field was considered in the radial range of $J/\sigma_o < r < 5J/\sigma_o$ and the angular range $|\theta| \leq 45^\circ$, leading to a distance independent second order term. This allows the crack-tip fields to be simplified as:

$$\sigma_{ij} = \sigma_{ij}(Q = 0) + Q\sigma_o\delta_{1j} \quad (2.22)$$

The physical interpretation of Equation (2.22) is that the near crack-tip fields are thoroughly characterized by the HRR field, which is the reference field wherein Q is considered zero, together with the parameter Q that quantifies the change in hydrostatic stress ahead of the crack-tip due to the constraint loss. On this basis, Q may be defined as:

$$Q = \frac{\sigma_{ij}(r, \theta)}{\sigma_o} - \frac{\sigma_{ij}(r, \theta)_{Q=0}}{\sigma_o} \quad \text{at } \theta = 0, r = \frac{2J}{\sigma_o} \quad (2.23)$$

The distance $r = 2J/\sigma_o$ from the crack-tip was chosen as it lies just outside the finite strain blunting zone (McMeeking & Parks, 1979) so that the definition of Q was applicable to both small and finite strain analyses.

Most importantly, the two-dimensional $J - T/Q$ theory requires the field to be deviatorically similar which means the shear stresses must remain identical under constraint loss, but direct stresses differ hydrostatically. Another important requirement is that within the microstructural-separation distance ahead of the crack front normally within $2J/\sigma_o \leq r \leq 5J/\sigma_o$, the stress difference Q is distance independent. These requirements would allow the fields to be ranked as a family of fields that change due to $Q\sigma_o$ (O'Dowd & Shih, 1991).